

1 **Receiver function mapping of the mantle transition zone beneath the Western**
2 **Alps: New constraints on slab subduction and mantle upwelling**

3

4 *Dongyang Liu^{a,b}, Liang Zhao^{a,b,*}, Anne Paul^c, Huaiyu Yuan^{d,e}, Stefano Solarino^f, Coralie Aubert^c,*
5 *Silvia Pondrelli^g, Simone Salimbeni^g, Elena Eva^f, Marco G. Malusa^{h,f}, Stéphane Guillot^c*

6 ^a State Key Laboratory of Lithospheric Evolution, Institute of Geology and Geophysics, Chinese
7 Academy of Sciences, Beijing 100029, China

8 ^b College of Earth and Planetary Sciences, University of Chinese Academy of Sciences, Beijing
9 100049, China

10 ^c Univ. Grenoble Alpes, Univ. Savoie Mont Blanc, CNRS, IRD, UGE, ISTERre, 38000 Grenoble,
11 France

12 ^d ARC Centre of Excellence for Core to Crust Fluid Systems, Department of Earth and
13 Environmental Sciences, Macquarie University, North Ryde, Australia

14 ^e Centre for Exploration Targeting, School of Earth Sciences, The University of Western Australia,
15 35 Stirling Highway, Crawley, Perth, Western Australia 6009, Australia

16 ^f Istituto Nazionale di Geofisica e Vulcanologia, Osservatorio Nazionale Terremoti, Genova, Italy

17 ^g Istituto Nazionale di Geofisica e Vulcanologia, Via Donato Creti 12, 40128 Bologna, Italy

18 ^h Department of Earth and Environmental Sciences, University of Milano-Bicocca, Milan, Italy

19 *Corresponding author at: State Key Laboratory of Lithospheric Evolution, Institute of Geology
20 and Geophysics, Chinese Academy of Sciences, Beijing 100029, China

21 E-mail address: zhaoliang@mail.iggcas.ac.cn (L.Zhao)

22

23 **Abstract¹**

24 To better constrain the deep structure and dynamics of the Western Alps, we studied the
25 mantle transition zone (MTZ) structure using P-wave receiver functions (RFs). We obtained a total
26 of 24904 RFs from 1182 events collected by 307 stations in the Western Alps. To illustrate the
27 influence of the heterogeneity on the upper mantle velocity, we used both IASP91 and
28 three-dimensional (3-D) velocity models to perform RF time-to-depth migration. We documented
29 an MTZ thickening of about 40 km under the Western Alps and most of the Po Plain due to the
30 uplift associated with the 410-km discontinuity and the depression associated with the 660-km
31 discontinuity. Based upon the close spatial connection between the thickened MTZ and the
32 location of the subducted slabs, we proposed that the thick MTZ was due to the subduction of the
33 Alpine slab through the upper MTZ and the presence of remnants of subducted oceanic
34 lithosphere in the MTZ. The uplift associated with the 410-km discontinuity provided independent
35 evidence of the subduction depth of the Western Alps slab. In the Alpine foreland in eastern
36 France, we observed localized arc-shaped thinning of the MTZ caused by a 12 km depression of
37 the 410-km discontinuity, which has not been previously reported. This depression indicated a
38 temperature increase of 120 K in the upper MTZ, and we proposed that it was caused by a
39 small-scale mantle upwelling. Hardly any uplift of the 660 km discontinuity was observed,
40 suggesting that the thermal anomaly was unlikely to be the result of a mantle plume. We observed
41 that the thinning area of the MTZ corresponded to the area with the highest uplift rate in the

¹**Abbreviations**

mantle transition zone (MTZ)

receiver function (RF)

common conversion point (CCP)

42 Western Alps, which may have indicated that the temperature increase caused by the mantle
43 upwelling contributed to the topographic uplift.

44

45 **Keywords:** Mantle transition zone, Subduction zone processes, Western Alps, Mantle processes,
46 Receiver functions.

47 **1 INTRODUCTION**

48 The mantle transition zone (MTZ) separates the upper mantle from the lower mantle over the
49 entire Earth. The MTZ has been widely studied because the topography of its upper and lower
50 boundaries inferred from geophysical observations can be linked to the results of mineral physics
51 in terms of the thermal state, mineralogy and/or water content of the transition zone. Subducting
52 plates and mantle convection induce phase transitions at the upper (410-km) and lower (660-km)
53 boundaries of the MTZ in the form of thermal perturbations, which can be traced as depth changes
54 in these discontinuities. Such depth variations provide clues to the structure and dynamics of the
55 upper mantle. The subduction depth of the Western Alps slab and the origin of the mantle flow
56 beneath and inside the mantle lid of the European Plate play crucial roles in our understanding of
57 the regional geodynamics. The rapid topographic uplift rates in the Western Alps are believed to
58 be partly due to mantle-related processes (Serpelloni et al., 2013; Nocquet et al., 2016; Sternai et
59 al., 2019). Therefore, we used receiver functions (RFs) to study the seismic characteristics of the
60 MTZ under the Western Alps, to provide new constraints on the depth penetration of the
61 subducted plate, and then discuss the geodynamic origin of the low-velocity anomaly behind the
62 subduction zone and its relationship with the present-day uplift rates in the Western Alps.

63 **1.1 MTZ under the Western Alps and adjacent areas**

64 The MTZ is bound by two global scale discontinuities at depths of 410 km and 660 km,
65 characterized by strong seismic velocity changes, which are mainly related to high-pressure phase
66 transitions of olivine in seismic properties. The 410-km discontinuity is associated with the
67 polymorphic phase transitions from olivine (α spinel) to wadsleyite (β spinel) in an exothermic
68 reaction with a positive Clapeyron slope. The 660-km discontinuity is associated with phase
69 transitions from ringwoodite (γ spinel) to bridgmanite and ferropericlase, in an endothermic
70 reaction with a negative Clapeyron slope. Therefore, a 100 K temperature decrease in the MTZ
71 induced the uplift of the 410-km discontinuity and the depression of the 660-km discontinuity, and
72 thus, about 10 km of thickening. Conversely, a thinner MTZ is expected in anomalously hot
73 regions. Lateral variations in the depths of the two seismic discontinuities provide important
74 information about the lateral temperature variations within the MTZ, and therefore, they can be
75 used to constrain the geometric characteristics of subducted plates and reflect the scale of mantle
76 convection.

77 Van der Meijde et al. (2005) studied the MTZ structure beneath a sparse station array in the
78 Mediterranean region using RFs. The only station they used in the Alps was in the southwestern
79 part of the belt. It revealed a thick MTZ, which Van der Meijde et al. (2005) explained as high
80 average seismic velocities in the MTZ. Lombardi et al. (2009) used data from 98 stations spread
81 over the Alpine region and reported an increase in the thickness of the MTZ of about 30–40 km in
82 a large zone covering the southwestern Alps and most of the Po Basin. Because this thickness
83 anomaly is due only to a subsidence of the 660-km discontinuity, Lombardi et al. (2009) proposed
84 that the 40 km of thickening was due to a strong temperature decrease of about 800 K in the lower
85 part of the MTZ. They attributed this cold anomaly to the presence of lithospheric slab remnants

86 from the Tethyan Ocean, which accumulated at the 660-km discontinuity. The European-scale
87 study of Cottaar and Deuss (2016) revealed large-scale 30 km depressions of the 660-km
88 discontinuity beneath central Europe, without any corresponding topographic variation in the
89 410-km discontinuity. Although they had good station coverage in the Alpine area, their results did
90 not confirm the strong anomaly in the 660-km discontinuity reported by Lombardi et al. (2009) in
91 the Western and Southern Alps. Liu et al. (2018) focused their RF analysis on the Alpine region to
92 investigate water transport through the MTZ in subduction zones. They suggested that the 660-km
93 discontinuity was depressed by 10–40 km beneath the south-central Alps, whereas the 410-km
94 discontinuity was not deflected appreciably. Liu et al. (2018) proposed that the depressed 660-km
95 discontinuity indicated that the subducted material had sunk to the bottom of the transition zone.
96 They also provided evidence of low-velocity zones (LVZs) above the 410-km discontinuity
97 beneath the regions near the Alpine subduction, such as northeastern France and the Ligurian Sea.
98 According to Liu et al. (2018), these LVZs outside of the Alps could be explained by melting
99 induced by water released from the MTZ in an ascending mass flow that compensated for the
100 descending flow caused by the spreading of the lithospheric slab remnants above the 660-km
101 discontinuity.

102 In this study, we used a much denser seismic array than those used in previous studies,
103 including permanent and temporary stations of the CIFALPS and CIFALPS-2 experiments (see
104 improvement in the mapping of the 410-km discontinuity in Fig. S1). In addition, we used a
105 three-dimensional (3-D) velocity model to calculate accurate ray paths and to correct the depth
106 estimates of the MTZ discontinuities in the structure of the upper mantle. The results of our study
107 provides new constraints and shed light on the topographic variations in the two discontinuities

108 over a broad region, including the Western Alps and the Alpine foreland in Eastern France.

109 **1.2 Tectonic background**

110 The Alpine orogenic belt is the result of continental collision and convergence between the
111 Adriatic microplate and the European Plate during the Mesozoic (Handy et al., 2010). During the
112 Cretaceous, most of the Tethys Ocean subducted below the Adriatic Plate (Dewey et al., 1989;
113 Malusà et al., 2015). With the progressive closure of the Tethys Ocean, subduction was blocked in
114 the Middle-Late Eocene. The Apenninic slab gradually moved northward and may have started
115 interacting with the European Plate from the Oligocene (Malusà et al., 2016). The Apenninic Plate
116 retreated eastward in the Neogene, resulting in the opening of the Ligurian sea (Jolivet and
117 Faccenna, 2000) and the associated counterclockwise rotation of Corsica-Sardinia in the
118 Apenninic backarc region (Fig. 1) (Lustrino et al., 2011). The Alpine orogenic belt has a complex
119 tectonic history, and the deformation in and around the Alps is controlled by the displacements of
120 several microplates (e.g., Adria and Iberia), which generated orogenic belts around the Alps,
121 particularly the Pyrenees, the Apennines, the Betics, and the Dinarides (Handy et al., 2010).

122 The seismic velocity anomalies in the mantle beneath the Western Alps have been analyzed
123 using various tomography models (Piromallo and Morelli, 2003; Lippitsch et al., 2003; Koulakov
124 et al., 2009; Zhu et al., 2012, 2015; Zhao et al., 2016a; Hua et al., 2017). Seismic tomography
125 studies of the crust and upper mantle beneath the Western Alps have mapped a dipping slab that
126 can be traced from the crust to the MTZ (e.g., Zhu et al., 2012; Zhao et al., 2016a; Hua et al.,
127 2017). This high-velocity anomaly has been interpreted as the Alpine slab in all publications.
128 Regional tomography results for the area beneath the central-western Mediterranean also revealed
129 that a large amount of high-velocity materials has accumulated in the MTZ, which resulted from

130 different subduction episodes (Piromallo and Morelli, 2003; Zhu et al., 2012). According to a
131 preliminary interpretation of the recent teleseismic tomography data obtained by Paffrath et al.
132 (2020), Agard and Handy (2021) proposed that the steeply dipping subducted slab is mostly of
133 European origin and that a gap exists in-between the subducted lithosphere with strong dip and the
134 slab remnants in the MTZ on the 660-km discontinuity. A low-velocity anomaly was imaged from
135 100 km to 250 km on the lower plate side of the Western Alps slab, extending with lower
136 amplitudes down to the transition zone (e.g., Koulakov et al., 2009; Zhao et al., 2016a), which was
137 attributed to thermal origin and may be linked to a counterflow induced by rollback of the
138 Apenninic slab (Zhao et al., 2016a; Malusà et al., 2021). Hua et al. (2017) proposed that the
139 high-velocity anomalies in the mantle under the Alps coexist with negative radial anisotropy,
140 which could be triggered by a subducting slab and the mantle flow it induced. In the Western Alps,
141 these mantle processes also may significantly contribute (~30%) to the observed surface uplift
142 rates predicted by modeling of the dynamic topography (Sternai et al., 2019). Therefore, the
143 Western Alps are an ideal location for studying the origin of the low-velocity anomaly behind the
144 subduction zone and its influence on the topography. Indeed, low-velocity anomalies behind
145 subduction zones have been observed not only in the Western Alps but also at the plate boundaries
146 in Japan (Wei and Shearer, 2017) and in the Western United States (Bodmer et al., 2018).

147

148 **2. Data and methods**

149 We used waveform data collected from 307 broadband seismic stations in the Western Alps
150 and adjacent foreland areas (Fig. 1b). In addition to the 197 stations that are part of the Swiss (CH),
151 French (FR, RD, G), and Italian (IV, GU) permanent networks, we used data from 110 temporary

152 stations set up for two experiments in the China-Italy-France Alps Seismic Survey (CIFALPS)
153 project. Both the CIFALPS and CIFALPS-2 experiments included 55 stations spaced about 5–10
154 km apart along transects through the southwestern Alps for the CIFALPS and the northwestern
155 Alps and the Ligurian Alps for CIFALPS-2. The CIFALPS stations operated for 13 months in
156 2012–2013 (Zhao et al., 2015, 2016b); and the CIFALPS-2 experiment operated for 14 months in
157 2018–2019 (Zhao et al., 2018). We selected events with epicentral distances of 30° - 90° and
158 magnitudes (M_w) of 5.3 to 9.0 for the period 2012–2019.

159 Assuming that the vertical component represents the source time function, we calculated the
160 RFs using time-domain interactive deconvolution of the vertical component from the radial
161 component (Ligorria and Ammon, 1999). The data were band pass filtered in the frequency band
162 of 0.02–0.5 Hz and windowed from 15 s before to 100 s after the predicted direct P-wave arrival
163 time. We employed an automatic screening criterion to select high-quality RFs: (1) the direct P
164 arrival should be within 1s of the zero-delay time; and (2) after the main P-wave, there should not
165 be another peak exceeding 70% of the P-wave amplitude. We calculated the correlation between
166 each individual receiver function and the average receiver function at the given station and
167 rejected the signals with correlation coefficients of less than 0.4. Then, the data were manually
168 checked for quality. After the quality check, we kept 24904 RFs from 1182 teleseismic events for
169 further analysis.

170 We used the common conversion point (CCP) stacking approach (Dueker and Sheehan, 1997)
171 to construct a 3-D image of the RFs with depth to map the topographic variations in the two
172 discontinuities. The CCP stacks were created using RFs from different sources and records from
173 different stations, but they sampled the same target region at depth. Before the stacking, we

174 divided the region under the Western Alps into small blocks (10 km × 10 km horizontally and 2
175 km in depth) from the surface to a depth of 800 km. For each conversion depth, we calculated the
176 piercing points and travel times of the converted Ps (P to S) phase through ray tracing within a
177 velocity model. We considered two reference velocity models, the IASP91 spherical Earth
178 reference model (Kennett and Engdahl, 1991) and the EU60 3-D model (Zhu et al., 2015), to
179 accurately locate the piercing points of the Ps phases and then to compute the moveout corrections.
180 The EU60 model is a 3-D crust and upper mantle velocity model computed from adjoint
181 tomography data, which constrains the absolute P-wave and S-wave velocities from the subsurface
182 to a depth of 1000 km (Zhu et al., 2015). Because of the inclusion of body waves, the ray coverage
183 of the EU60 model can be extended to the MTZ. The P-wave velocity variations at 410 km and
184 660 km and the V_p/V_s ratio at 600 km in the EU60 model are shown in Fig. 2. It is possible to
185 observe the high-velocity anomalies below the Po Plain, a low-velocity anomaly around the
186 orogenic belt at 410 km (Fig. 2a), and a high-velocity anomaly at 660 km (Fig. 2b). Similar
187 anomalies have been imaged in other tomography studies (Piromallo and Morelli, 2003; Koulakov
188 et al., 2009; Zhao et al., 2016a).

189 With the improvements in the accuracy and resolution of tomographic models, 3-D velocity
190 models have been used to migrate RF data. To calculate the mantle corrections to the relative Ps
191 travel times, we first computed the true 3-D ray paths based on the EU60 velocity model using the
192 fast-marching method (Rawlinson et al., 2005). Then, we divided each ray into depth segments
193 and calculated the travel time for each ray segment according to the EU60 model. The amplitudes
194 of the RFs were back-projected to the grid points corresponding to the ray paths according to their
195 relative arrival times and were stacked into nearby grid points using a weighting factor that

196 depends on the half width of the Fresnel zone at the corresponding depth (Test. S1 in the
197 Supporting Information). To check the validity of the method, we designed two 1-D synthetic tests
198 by adding a 100 km thick layer with an anomalous velocity in the upper mantle and in the MTZ
199 (Fig. S2). Then, we applied the 1-D and 3-D correction methods, and the results showed the
200 discontinuities were well recovered by the 3-D velocity corrections. Fig. 3 shows the geographic
201 layout of the piercing points of the Ps conversions at the two discontinuities obtained using the
202 3-D velocity model, which indicates that the coverage of the study region was good.

203

204 **3 Results**

205 In general, the Ps conversions from the two discontinuities were prominent in the cross
206 sections of the CCP stacks obtained using the IASP91 model (Fig. S3). The depression of the
207 660-km was quite visible in all sections, and it gradually approached the average global depth
208 toward the north (Test. S2). Both uplift and depression were observed in different areas of the
209 410-km discontinuity. The amplitudes of the converted P410s phase weaken significantly in the
210 north part of the study area, where P410s became hard to detect.

211 Maps of the discontinuity's topography were drawn by picking the depths of the maximum
212 amplitudes of the RFs within the respective depth ranges of 380–440 km and 630–710 km. We
213 found that the average depths of the two discontinuities were 414 ± 10.3 km and 673 ± 5.9 km for
214 the IASP91 model (Figs. 4a and 4b). Figs. 5a and 5b showed the topographies of the two
215 discontinuities estimated using the IASP91 model. A striking feature of the topographic maps was
216 the depressed 660-km discontinuity across the entire study area, which was suggested by the CCP
217 profiles (Fig. S3). The most prominent depth anomaly was located in the southern part of the

218 mountain belt, where the 660-km discontinuity was about 30 km deeper than normal. As proposed
219 in previous studies, the depressed 660-km discontinuity may be related to the widespread
220 accumulation of cold materials in the MTZ (Lombardi et al., 2009). In contrast, the 410-km
221 discontinuity was depressed in a large area to the north and west of the mountain belt, while the
222 discontinuity is uplifted by about 10 km to 20 km beneath the Po Plain (Fig. 5a).

223 Figs 5d and 5e showed the depth variations of the two discontinuities corrected using the
224 EU60 3-D P- and S-wave absolute velocity model. After the 3-D velocity corrections, the average
225 depths of the two discontinuities were found to be 412 ± 9.3 km and 675 ± 5.7 km (Figs. 4c and 4d).
226 For most of the study area, overall, the depth changes of the discontinuities corrected using the
227 EU60 velocity heterogeneities were similar to those corrected using the IASP91 model (Figs. 5a,
228 5b, 5d, 5e). The main difference was the absolute depth of the discontinuities. The depth of the
229 depressed 410-km discontinuity was corrected by a maximum of 12 km, which was a result of
230 accounting for the low-velocity anomaly in the tomography of the EU60 (Fig. 2a). Therefore, the
231 topographic relief and the standard deviation on the depth of the 410-km discontinuity were
232 smaller for the EU60 model than for the IASP91 model (Figs. 4a, 4c, 5a, and 5d). The depths of
233 the 660-km discontinuity were greater after correction using the EU60 model, with a maximum
234 correction of 5 km, which corresponded to the correction for the high-velocity anomalies in the
235 MTZ (Fig. 2b). This depth correction was consistent with the velocity variations in the EU60
236 model. We calculated the standard errors on the depths of the discontinuities, which were less than
237 5 km in most areas (Fig. S4). Therefore, based on the good data coverage of our study (Figs. 3a
238 and 3b) and the fair resolution of the EU60 model in the study area, we are confident that the
239 depth variations of the two discontinuities were robustly estimated.

240 The thickness of the MTZ was obtained by subtracting the depth of the 410-km discontinuity
241 from the depth of the 660-km discontinuity in overlapping CCP bins to eliminate uncertainties
242 caused by migration using an inaccurate velocity model in the upper mantle. The MTZ thickness
243 maps created using the IASP91 model and the EU60 model were similar (Figs. 5c and 5d). The
244 most prominent anomaly was the thickening of the transition zone beneath the Western Alps and
245 the Po Plain. The MTZ was approximately 25–40 km thicker than the global average of 250 km in
246 the IASP91 Earth model, which corresponded to the locally depressed 660-km discontinuity and
247 uplifted 410-km discontinuity shown in Figs. 5d and 5e. The 12 km (on average) thinning of the
248 MTZ occurred in the Alpine foreland of Eastern France (Fig. 5f). These variations in the thickness
249 were correlated with the velocity structure of the MTZ. The MTZ tended to be thicker where the
250 velocities were higher, and thinner where the velocities were lower (Figs. 2a and 2b).

251 Fig. 6 compares the CCP stacked cross sections with the P-wave tomographic model of Zhao
252 et al. (2016a) along the transects in the southwestern Alps (section a-A) and in the northwestern
253 Alps (section b-B). In both cross sections, the depression of the 410-km discontinuity in the west
254 correlated well with the low-velocity anomalies extending to the MTZ revealed by the P-wave
255 tomography model. The high-velocity anomaly in the east matched the uplift of the 410-km
256 discontinuity well.

257 **4 Discussion**

258 Using an accurate 3-D velocity model of the mantle should lead to more accurate estimates of
259 the depths of two discontinuities and the thickness of the MTZ and thus to more accurate
260 information about the temperature anomalies in the MTZ. In this section, we used the corrected
261 depths of the discontinuities to constrain the subduction depth of the Western Alps slab, and we

262 discussed the causes of the depression of the 410-km as well as the possible link between the
263 mantle convection and topographic uplift.

264 **4.1 Cold slabs in the MTZ beneath the Western Alps**

265 The most salient anomaly in the MTZ was the 15–40 km increase in its thickness below the
266 Western Alps and the Po Plain, with an average increase in thickness of about 28 km. The
267 thickening of the MTZ was caused by the 10 km uplift of the 410-km discontinuity and the 30 km
268 depression of the 660-km discontinuity. According to the synthetic test shown in Fig. S5, a 10-km
269 anomaly could be identified from the RFs. In the following, we used Clapeyron slopes of +2.5
270 MPa·K⁻¹ (Katsura and Ito, 1989) and -2.9 MPa·K⁻¹ (Yu et al., 2007) for the 410-km and 660-km
271 discontinuities, respectively. The 40 km thickening was related to a -300 K temperature anomaly
272 in the MTZ as compared with the global average. Using the scaling parameter $dV_p/dT = -4.8 \times$
273 $10^{-4} \text{ km} \cdot \text{s}^{-1} \cdot \text{K}^{-1}$ (Deal et al., 1999), the corresponding V_p anomaly in the MTZ was about +1.4%,
274 which was in agreement with the high-velocity anomalies in the EU60 model (Fig. 2b). In addition,
275 given that the depression of the 660-km discontinuity was the main reason for the thickening of
276 the MTZ, we predicted a stronger temperature decrease of up to -450 K at the base of the MTZ,
277 which would explain the 30 km depression of the 660-km discontinuity. This finding was
278 consistent with the temperature decrease (350–450 K) in the MTZ inferred from deep
279 magnetotelluric sounding data collected in the French Alps (Tarits et al., 2004).

280 Based upon the model corrected using the EU60, the uplifted 410-km discontinuity could be
281 interpreted in terms of the low temperatures associated with the subducted Western Alps slab (Fig.
282 5d). Piromallo and Faccenna (2004) estimated that the convergence of Adria and Europe has
283 resulted in at least 400 km of horizontal shortening in the Western Alps during the past 67 Ma

284 according to plate-tectonic reconstruction results (Dewey et al., 1989). Zhu et al. (2012) suggested
285 that the maximum subduction depth, revealed by their adjoint tomography model, is nearly 400
286 km beneath the Alpine belt. The teleseismic tomography of Zhao et al. (2016a) revealed a strongly
287 dipping high-velocity anomaly that could be continuously traced to a depth of 400 km in the
288 Western Alps, whereas a positive velocity anomaly of about +1% was still visible at a depth of
289 ~420 km. Hua et al. (2017) suggested that the maximum depth of the subducted slab in the
290 Western and Central Alps was ~450 to 500 km. The observed uplift of the 410-km discontinuity
291 under the Western Alps may have indicated that the present-day subducted plate passed through
292 the 410-km discontinuity and entered the MTZ (Figs. 5d and 6), providing an additional constraint
293 on the maximum subduction depth of the Western Alps slab.

294 The depressed 660-km discontinuity indicated that cold subducted materials have
295 accumulated at this discontinuity (Fig. 7). Tomographic images (Piromallo and Morelli, 2003; Zhu
296 et al., 2012) have revealed a broad high-velocity zone in the MTZ in the Central-Western
297 Mediterranean. Piromallo and Faccenna (2004) and Zhu et al. (2012) suggested that these
298 large-scale anomalies may be pieces of the subducted Alpine Tethys oceanic lithosphere, which
299 were conveyed to the MTZ by various subduction events and piled up at a depth of 660 km.
300 Previous seismic studies of the MTZ under the Alpine region reported that the 660-km
301 discontinuity was the only contributor to the thickening of the MTZ and was the only phase
302 transition affected by the cold plate (Lombardi et al., 2009; Cottaar and Deuss, 2016; Liu et al.,
303 2018). We have documented, however, that the uplifted 410-km discontinuity also contributed to
304 the thickening of the MTZ. Therefore, the thicker transition zone beneath the Western Alps
305 provided evidence not only of the presence of mantle lithosphere slab remnants above the 660-km

306 discontinuity, as suggested by tomography studies (Piromallo and Morelli, 2003; Zhu et al., 2015),
307 but also for the maximum depth reached by the high-velocity anomaly corresponding to the Alpine
308 subduction.

309 In addition to temperature anomalies, a high-water content could also cause the thickening of
310 the MTZ (Litasov et al., 2005). Studies have proposed that an increase in the water content of
311 ringwoodite could reduce the V_s significantly, while having little effect on the V_p , and thereby
312 increasing the V_p/V_s ratio (Jacobsen and Smyth, 2006). Seismic tomography studies have
313 revealed an increase rather than a decrease in the S-wave velocity within the MTZ beneath the
314 Western Alps (e.g., Utada et al., 2009; Zhu et al., 2015). Moreover, the V_p/V_s ratio does not
315 increase at a depth of 600 km in the EU60 model (Fig. 2c) (Cottaar and Deuss, 2016). An
316 increased water content also could broaden the depth interval of the phase transition, leading to an
317 increase in the attenuation and low amplitude RFs (Wood, 1995). We did not observe, however, a
318 decrease in the amplitude of the depressed 660-km discontinuity (Fig. S3). In addition, the
319 electrical conductivity study conducted by Utada et al. (2009) revealed a low conductivity under
320 the Mediterranean region at depths of 400–700 km, which correlated well with the high-velocity
321 anomalies. Therefore, the hypothesis that the depression of the 660-km discontinuity was related
322 to the widespread distribution of hydrous minerals was unlikely.

323 **4.2 A hot MTZ surrounding the Western Alps slab**

324 The map of the corrected MTZ thickness showed a thinner MTZ in the northwestern part of
325 the Western Alps, which was caused mainly by the arc-shaped depression of the 410-km
326 discontinuity around the arc-shaped Western Alps (Fig. 5). Because the 410-km discontinuity was
327 more depressed than the 660-km discontinuity, the MTZ was 12 km thinner than the global

328 average of 250 km, with a maximum thinning of 23 km. The depression of the 410-km
329 discontinuity observed on the depth map corrected using the 3-D EU60 model (Fig. 5d) was not an
330 artifact caused by an inaccurate velocity correction because it also was observed when the IASP91
331 1-D model was used for the migration (Fig. 5c). A low-velocity anomaly has been identified in
332 various tomography studies of the area surrounding the Western Alps slab (Koulakov et al., 2009;
333 Zhao et al., 2016a; Hua et al., 2017). New shear-wave splitting observations led Salimbeni et al.
334 (2018) to propose that the low-velocity anomalies at the rear of the Western Alps slab have a
335 thermal origin and may have generated the vertical component of the mantle counterflow induced
336 by the retreat of the Apenninic slab to the south. The low-velocity anomalies can be traced from
337 100 km to 250 km depth and they extend with lower amplitudes down to the MTZ, which
338 corresponded to the depressed 410-km discontinuity (e.g., Koulakov et al., 2009; Zhao et al.,
339 2016a). The 12 km average thinning of the MTZ was mainly the results of the depressed 410-km
340 discontinuity, which indicated a +120 K thermal anomaly at the 410-km discontinuity for a
341 Clapeyron slope of $+2.5 \text{ MPa}\cdot\text{K}^{-1}$. Using the scaling parameter $dV_p/dT = -4.8 \times 10^{-4} \text{ km}\cdot\text{s}^{-1}\cdot\text{K}^{-1}$
342 (Deal et al., 1999), the positive thermal anomaly led to a -0.6% velocity reduction, which was
343 consistent with the results of previous seismic tomography studies (Koulakov et al., 2009; Zhu et
344 al., 2015; Zhao et al., 2016a).

345 The slightly thinner MTZ caused by the larger depression of the 410-km compared with that
346 of the 660-km discontinuity may have been due to the thermal anomaly in the upper part of the
347 MTZ. It may represent small-scale mantle flow that would transport the hotter material of the
348 MTZ into the upper mantle and induce a temperature increase. The depressed 410-km
349 discontinuity was distributed outside of the Western Alps and parallel to the arc-shaped trend of

350 the orogenic belt (Fig. 5d). We proposed that the mantle flow pattern at the rear of the Western
351 Alps slab was composed of two components: (1) toroidal flow, that is, a counterflow induced by
352 the Apenninic slab retreating to the southeast (Salimbeni et al., 2018; Malusà et al., 2021); and (2)
353 poloidal flow and associated upwelling. The numerical simulations suggested that this upwelling
354 usually was part of the return flow system caused by active slab subsidence (Faccenna et al., 2010).
355 Therefore, a major cause of contributing to this thermal anomaly may be the downwelling of the
356 Alpine lithosphere, which induced poloidal return flow in the surrounding mantle. On the basis of
357 the observations that the Alpine subduction extended to the depth of the MTZ and that cold
358 subducted materials accumulated in the MTZ at the 660-km discontinuity, the quasi-vertical
359 Alpine subduction may have induced two poloidal flow cells, one underneath the subducting plate
360 and the other one in the mantle wedge above the plate. This flow pattern would be caused by the
361 shearing between the plate and the mantle because of the inclined plate parallel component of the
362 displacement and could be better observed in vertical subduction (Schellart, 2004). Like the
363 Western Alps, the thinning of the transition zone under the Pacific Coast of North America also
364 was due to a more depressed 410-km as compared with the 660-km discontinuity, which indicated
365 that the temperature in the upper part of the MTZ was higher (Gao and Liu, 2014). Bodmer et al.
366 (2018) attributed the low-velocity anomaly along the Cascadia forearc to mantle upwelling and to
367 a thermally buoyant mantle.

368 **4.3 Relationship between topographic uplift and mantle upwelling**

369 The Western Alps contain the highest peaks in Europe and have a higher average elevation
370 than other segments of the Alpine orogen belt. However, the detailed mechanisms that control
371 their surface uplift are not well understood. Global Positioning System (GPS) and leveling have

372 revealed that the present-day uplift rates of the Alps are $1\text{--}2\text{ mm}\cdot\text{yr}^{-1}$, with the maximum uplift rate
373 mainly occurring in the Western Alps ($> 2\text{ mm}\cdot\text{yr}^{-1}$; Serpelloni et al., 2013, Nocquet et al., 2016).
374 This high uplift rate cannot be explained simply by the ongoing convergence between the Adriatic
375 microplate and the European Plate, nor can it be attributed solely to the postglacial rebound and
376 erosion. Several studies have proposed that the present-day surface dynamics also are controlled
377 by deep-seated processes (Serpelloni et al., 2013; Nocquet et al., 2016; Salimbeni et al., 2018;
378 Sternai et al., 2019). Indeed, the elevation change in an orogenic belt has been dynamically
379 controlled by the mantle convection at the edges of the converging plates (Faccenna and Becker,
380 2010). In the Mediterranean region, Faccenna et al. (2010) proposed that small-scale convection
381 was the engine of the dynamic topography and microplate motions. Previous studies (Sue et al.,
382 1999; Fox et al., 2015) have suggested that the high uplift and erosion rates may have been due to
383 a surface response to slab breakoff under the Western Alps. However, this explanation has been
384 questioned based on recent tomographic results, which have revealed a continuous high-velocity
385 anomaly beneath the Western Alpine region that can be traced to the MTZ (Zhao et al., 2016a;
386 Hua et al., 2017). Sternai et al. (2019) evaluated the relative contributions of the different velocity
387 perturbation models (Lippitsch et al., 2003; Zhao et al., 2016a) to the observed vertical
388 displacement rates at the surface and suggested that deglaciation and erosion account for about
389 half of the observed uplift rate in the Western Alps. Regarding the mantle convection mechanism,
390 although the absolute magnitude of its contribution to the uplift rate is difficult to independently
391 evaluate based on existing knowledge, the mantle flow may have made a significant contribution
392 of about 10–30% to the uplift rate at the orogen scale (Sternai et al., 2019) considering the
393 velocity perturbation model by Zhao et al. (2016a).

394 With the subduction of the Alpine lithosphere, the downwelling of the lithospheric mantle
395 into the deeper mantle may cause a return flow system, leading to mantle upwelling. We propose
396 that the depression of the 410-km along the edge of the orogenic belt was the result of these
397 small-scale mantle flows, which have transported hotter material from the MTZ into the upper
398 mantle. Due to the lack of the toroidal flow between the northern end of the Apenninic subduction
399 and the southwestern end of the Alpine subduction, the rollback of the Apenninic slab may have
400 induced a suction effect and an asthenospheric counterflow around the northwestern part of the
401 subducted European slab during the Neogene (Salimbeni et al., 2018; Malusà et al., 2021). We
402 speculate that the vertical component of the mantle flow gradually propagated toward the
403 southeast along the edge of the Alpine slab due to the suction effect caused by the rollback of the
404 Apenninic slab (Fig. 7). Therefore, the mantle upwelling exhibited an oblique upward propagation
405 path in the upper mantle (Figs. 6 and 7). In particular, Fig. 5f shows the good spatial agreement
406 between the thinned area of the MTZ and the region of topographic uplift (green lines) under the
407 constraint of this propagation path in the Western Alps. In addition to the upwelling from the MTZ,
408 we noticed that the asthenosphere also was the source of the temperature increase in the external
409 regions of the Western Alps Plate. Therefore, we suggested that the heat flow from the MTZ
410 propagated upward, resulting in an increase in the temperature behind the Alpine slab. The
411 low-velocity anomaly observed by the tomography results can be explained by such a thermal
412 anomaly. When the upwelling reaches the bottom of the lithosphere at an estimated depth of 100
413 km (Lyu et al., 2017), it interacted with the overlying cold, dense mantle material, triggering
414 surface uplift. This hypothesis can explain why the average elevation and the peaks of the Western
415 Alps are higher than those of the other segments of the orogen, but further study is needed to

416 verify this hypothesis. In addition to the occurrence of this phenomenon in the Western Alps, the
417 contribution of a low-velocity anomaly behind the slab to the topographic uplift also was proposed
418 in the Western United States by Bodmer et al. (2018, 2020). They proposed that a positive mantle
419 buoyancy zone caused by local upwelling promoted the topographic uplift of the Cascadia
420 Mountains by changing the slab dip or increasing the mechanical plate coupling.

421 **5. Conclusions**

422 We used 24904 high-quality RFs to investigate the topography of the MTZ discontinuities
423 under the Western Alps and the surrounding areas. To obtain the absolute depths and improve the
424 accuracy of the time-to-depth migrations, we used the 3-D EU60 velocity model to correct the ray
425 paths and travel times in the upper mantle. We showed that the topographic relief of the two
426 discontinuities was reduced by the correction for 3-D velocity heterogeneities. Compared with
427 previous studies, our results confirmed that the thickening of the MTZ under the Western Alps
428 cannot be solely attributed to the depression of the 660-km, and it also was caused by the uplift of
429 the 410-km discontinuity. The uplifted 410-km may have been the result of the subduction of the
430 Alpine slab to the depth of the upper MTZ, which provides an important constraint on the
431 maximum present-day subduction depth of the Western Alps slab. As has been proposed in
432 previous publications, the depression of the 660-km discontinuity may be linked to the remnants
433 of oceanic lithosphere subducted during the closure of the Tethys Ocean. The most salient results
434 of our study include the depression of the 410-km discontinuity and the thinning of the MTZ
435 around the orogenic belt, which we attributed to a +120 K thermal anomaly caused by small-scale
436 mantle upwelling. Due to the lack of uplift in the 660-km discontinuity, the possibility that the
437 associated thermal anomaly originated from a mantle plume in the lower mantle can be excluded.

438 Our results indicated good agreement between the thinned area of the MTZ and the area of the
439 observed topographic uplift, which we ascribed to a temperature increase promoted by mantle
440 upwelling.

441 **Acknowledgement**

442 This research is funded by the National Natural Science Foundation of China (Grant
443 41625016, 41888101, and 91955210) and the National Key R&D Program of China (Grant
444 No.2017YFC0601201). The data of the two CIFALPS project were provided by the data centers of
445 the IGGCAS (Institute of Geology and Geophysics, Chinese Academy of Sciences) and the RESIF
446 (French seismic and geodetic network). The data of the permanent stations were provided by the
447 EIDA (European Integrated Data Archive). Most of them come from the Switzerland
448 Seismological Network, RESIF, and other broadband permanent networks in metropolitan France,
449 Regional Seismic Network of Northwestern Italy and Italian National Seismic Network. HY
450 acknowledges the Western Australian Exploration Incentive Scheme (EIS). This is contribution
451 xxx from the ARC Centre of Excellence for Core to Crust Fluid Systems
452 (<http://www.ccfs.mq.edu.au>).

453 **References**

454 Agard, P., Handy, M.R., 2021. Ocean Subduction Dynamics in the Alps. *Elements*. 17, 101–108.

455 Bodmer, M., Toomey, D.R., Hooft, E.E.E., Schmandt, B., 2018. Buoyant asthenosphere beneath
456 Cascadia influences megathrust segmentation. *Geophys. Res. Lett.* 45, 6954–6962.

457 Bodmer M, Toomey D.R., Roering J.J., Karlstrom L., 2020. Asthenospheric buoyancy and the
458 origin of high-relief topography along the Cascadia forearc. *Earth Planet. Sci. Lett.* 531,
459 1–10.

460 Cottaar, S., Deuss, A., 2016. Large-scale mantle discontinuity topography beneath Europe:
461 Signature of akimotoite in subducting slabs. *J. Geophys. Res. Solid Earth* 121, 279–292.

462 Deal, M.M., Nolet, G., van der Hilst, R.D., 1999. Slab temperature and thickness from seismic
463 tomography: 1. Method and application to Tonga, *J. Geophys. Res.*, 104 (B12),
464 28789–28802.

465 Dewey, J.F., Helman, M.L., Knott, S.D., Turco, E., Hutton, D.H.W., 1989. Kinematics of the
466 western Mediterranean. *Geol. Soc. (Lond.) Spec. Publ.* 45, 265–283.

467 Dueker, K.G., Sheehan, A.F., 1998. Mantle discontinuity structure beneath the Colorado Rocky
468 Mountains and high plains. *Geophys. Res: Solid Earth*, 103 (B4), 7153–7169.

469 Faccenna, C., Becker, T.W., 2010. Shaping mobile belts by small scale convection. *Nature* 465,
470 505–602.

471 Faccenna, C., Becker, T.W., Lallenmand, S., Lagabrielle, Y., Funicello, F., Piromallo, C., 2010.
472 Subduction-triggered magmatic pulses: A new class of plumes? *Earth Planet. Sci. Lett.* 299,
473 54–68.

474 Fox, M., Herman, F., Kissling, E., Willett, S.D., 2015. Rapid exhumation in the Western Alps
475 driven by slab detachment and glacial erosion. *Geology* 43, 379–382.

476 Gao, S.S., Liu, K.H., 2014. Mantle transition zone discontinuities beneath the contiguous United
477 States. *J. Geophys. Res. Solid Earth* 119, 6452–6468.

478 Handy, M.R., Schmid, S.M., Bousquet, R., Kissling, E., Bernoulli, D., 2010. Reconciling
479 plate-tectonic reconstructions of Alpine Tethys with the geological-geophysical record of
480 spreading and subduction in the Alps. *Earth Sci. Rev.* 102, 121–158.

481 Hua, Y., Zhao, D., Xu, Y., 2017. P wave anisotropic tomography of the Alps. *J. Geophys. Res.*

482 Solid Earth 122, 4509–4528.

483 Jacobsen, S.D., Smyth, J.R., 2006. Effect of water on the sound velocities of Ringwoodite in the
484 transition zone. In: Jacobsen, S.D., van der Lee, S. (Eds.), AGU Monograph 168 "Earth's
485 Deep Water Cycle", pp. 131–145.

486 Jolivet, L., Faccenna, C., 2000. Mediterranean extension and the Africa-Eurasia collision.
487 Tectonics. 19, 1095–1106.

488 Katsura, T., Ito, E., 1989. The system Mg_2SiO_4 - Fe_2SiO_4 at high pressures and temperatures:
489 Precise determination of stabilities of olivine, modified spinel, and spinel. J. Geophys. Res.
490 94, 15663–15670.

491 Kennett, B.L.N., Engdahl, E.R., 1991. Traveltimes for global earthquake location and phase
492 identification. Geophys. J. Int. 105, 429–465.

493 Koulakov, I., Kaban, M.K., Tesauro, M., Cloetingh, S., 2009. P and S velocity anomalies in the
494 upper mantle beneath Europe from tomographic inversion of ISC data. Geophys. J. Int.
495 179(1), 345–366.

496 Ligorría, J.P., Ammon, C.J., 1999. Iterative deconvolution and receiver-function estimation. Bull.
497 Seismol. Soc. Am. 89 (5), 1395 – 1400.

498 Lippitsch, R., Kissling, E., Ansorge, J., 2003. Upper mantle structure beneath the Alpine orogen
499 from high-resolution teleseismic tomography. J. Geophys. Res. 108(B8), 2376.

500 Litasov, K. D., Ohtani, E., Sano, A., Suzuki, A., Funakoshi K., 2005. Wet subduction versus cold
501 subduction. Geophys. Res. Lett. 32, L13312.

502 Liu, Z., Park, J., Karato, S., 2018. Seismic evidence for water transport out of the mantle transition
503 zone beneath the European Alps. Earth Planet. Sci. Lett. 482, 93–104.

504 Lombardi, D., Braunmiller, J., Kissling, E., Giardini, D., 2009. Alpine mantle transition zone
505 imaged by receiver functions. *Earth Planet. Sci. Lett.* 278 (3), 163–174.

506 Lustrino, M., Duggen, S., Rosenberg, C.L., 2011. The Central-Western Mediterranean: Anomalous
507 igneous activity in an anomalous collisional tectonic setting. *Earth Sci. Rev.* 104, 1–40.

508 Lyu, C., Pedersen, H.E., Paul, A., Zhao, L., Solarino, S., the CIFALPS Working Group, 2017.
509 Shear wave velocities in the upper mantle of the Western Alps: new constraints using array
510 analysis of seismic surface waves. *Geophys. Res. Lett.* 210, 321–331.

511 Malusà, M.G., Faccenna, C., Baldwin, S.L., Fitzgerald, P.G., Rossetti, F., Balestrieri, M.L., Danišić
512 K, M., Ellero, A., Ottria, G., Piromallo, C., 2015. Contrasting styles of (U)HP rock
513 exhumation along the Cenozoic Adria-Europe plate boundary (Western Alps, Calabria,
514 Corsica). *Geochem. Geophys. Geosyst.* 16, 1786–1824.

515 Malusà, M.G., Anfinson, O.A., Dafov, L.N., Stockli, D.F., 2016. Tracking Adria indentation
516 beneath the Alps by detrital zircon U-Pb geochronology: Implications for the
517 Oligocene-Miocene dynamics of the Adriatic microplate. *Geology* 44(2), 155–158.

518 Malusà, M.G., Guillot, S., Zhao, L., Paul, A., Solarino, S., Dumont, T., Schwartz, S., Aubert, C.,
519 Baccheschi, P., Eva, E., Lu, Y., Pondrelli, S., Salimbeni, S., Sun, W., Yuan, H., 2021. The
520 Deep Structure of the Alps Based on the CIFALPS Seismic Experiment: A Synthesis.
521 *Geochemistry, Geophysics, Geosystems.* 22, e2020GC009466.

522 Nocquet, J.M., Sue, C., Walpersdorf, A., Tran, T., Lenôtre, N., Vernant, P., Cushing, M., Jouanne,
523 F., Masson, F., Baize, S., Chéry, J., van der Beek, P.A., 2016. Present-day uplift of the
524 western Alps. *Sci. Rep.* 6, 28404.

525 Paffrath, M., Friederich, W. and the AlpArray Working Group, 2020. Teleseismic P-wave travel

526 time tomography of the Alpine upper mantle using AlpArray seismic network data, EGU
527 General Assembly 2020, Online, 4 – 8 May 2020, EGU2020-13779.

528 Piromallo, C., Faccenna, C., 2004. How deep can we find the traces of Alpine subduction?
529 *Geophys. Res. Lett.* 31, L06605.

530 Piromallo, C., Morelli, A., 2003. P wave tomography of the mantle under the
531 Alpine-Mediterranean area. *J. Geophys. Res.* 108(B2), 2065.

532 Rawlinson, N., Sambridge, M., 2005. The fast marching method: an effective tool for
533 tomographic imaging and tracking multiple phases in complex layered media. *Exploration*
534 *Geophysics* 36, 341–350.

535 Salimbeni, S., Malusà, M.G., Zhao, L., Guillot, S., Pondrelli, S., Margheriti, L., Paul, A., Solarino,
536 S., Aubert, C., Dumont, T., Schwartz, S., Wang, Q., Xu, X., Zheng, T., Zhu, R., 2018. Active
537 and fossil mantle flows in the western Alpine region unravelled by seismic anisotropy
538 analysis and high-resolution P wave tomography. *Tectonophysics* 731–732, 35–47.

539 Serpelloni, E., Faccenna, C., Spada, G., Dong, D., Williams, S.D., 2013. Vertical GPS ground
540 motion rates in the Euro-Mediterranean region: new evidence of velocity gradients at
541 different spatial scales along the Nubia-Eurasia plate boundary. *J. Geophys. Res.* 118,
542 6003–6024.

543 Schellart, W.P., 2004. Kinematics of subduction and subduction-induced flow in the upper mantle.
544 *J. Geophys. Res., Solid Earth* 109 (b7), b07401.

545 Sternai, P., Sue, C., Husson, L., Serpelloni, E., Becker, T.W., Willett, S.D., Faccenna, C., DiGiulio,
546 A., Spada, G., Jolivet, L., Valla, P., Petit, C., Nocquet, J.M., Walpersdorf, A., Castellort, S.,
547 2019. Present-day uplift of the European Alps: evaluating mechanisms and models of their

548 relative contributions. *Earth Sci. Rev.* 190, 589–604.

549 Sue, C., Thouvenot, F., Fréchet, J., Tricart, P., 1999. Widespread extension in the core of the
550 western Alps revealed by earthquake analysis. *J. Geophys. Res.* 104, 25611–25622.

551 Tarits, P., Hautot, S., Perrier, F., 2004. Water in the mantle: Results from electrical conductivity
552 beneath the French Alps. *Geophys. Res. Lett.* 31, L06612.

553 Utada, H., Koyama, T., Obayashi, M., Fukao, Y., 2009. A joint interpretation of electromagnetic
554 and seismic tomography models suggests the mantle transition zone below Europe is dry.
555 *Earth Planet. Sci. Lett.* 281(3-4), 249–257.

556 van der Meijde, M., van der Lee, S., Giardini, D., 2005. Seismic discontinuities in the
557 Mediterranean mantle. *Phys. Earth Planet. Inter.* 148, 233–250.

558 Wei, S.S., Shearer, P.M., 2017. A sporadic low-velocity layer atop the 410 km discontinuity
559 beneath the Pacific Ocean. *J. Geophys. Res. Solid Earth* 122, 5144–5159.

560 Wood, B.J., 1995. The effect of H₂O on the 410-kilometer seismic discontinuity. *Science* 268,
561 74–76.

562 Yu, Y.G., Wentzcovitch, R.M., Tsuchiya, T., Umemoto, K., Weidner, D.J., 2007. First principles
563 investigation of the postspinel transition in Mg₂SiO₄. *Geophys. Res. Lett.* 34, L10306.

564 Zhao, L., Paul, A., Guillot, S., Solarino, S., Malusà, M.G., Zheng, T.Y., Aubert, C., Salimbeni, S.,
565 Dumont, T., Schwartz, S., Zhu, R.X., Wang, Q.C., 2015. First seismic evidence for
566 continental subduction beneath the Western Alps. *Geology* 43, 815–818.

567 Zhao, L., Paul, A., Malusà, M.G., Xu, X., Zheng, T., Solarino, S., Guillot, S., Schwartz, S.,
568 Dumont, T., Salimbeni, S., Aubert, C., Pondrelli, S., Wang, Q., Zhu, R., 2016a. Continuity of
569 the Alpine slab unraveled by high-resolution P wave tomography. *J. Geophys. Res. Solid*

570 Earth 121, 8720–8737.

571 Zhao, L., Paul, A., Solarino, S., RESIF., 2016b. Seismic network YP: CIFALPS temporary
572 experiment (China-Italy-France Alps seismic transect) [Data set]. RESIF - Réseau
573 Sismologique et géodésique Français. <https://doi.org/10.15778/RESIF.YP2012>

574 Zhao, L., Paul, A., Solarino, S., RESIF., 2018. Seismic network XT: CIFALPS-2 temporary
575 experiment (China-Italy-France Alps seismic transect #2 [Data set]. RESIF - Réseau
576 Sismologique et géodésique Français. <https://doi.org/10.15778/RESIF.XT2018>

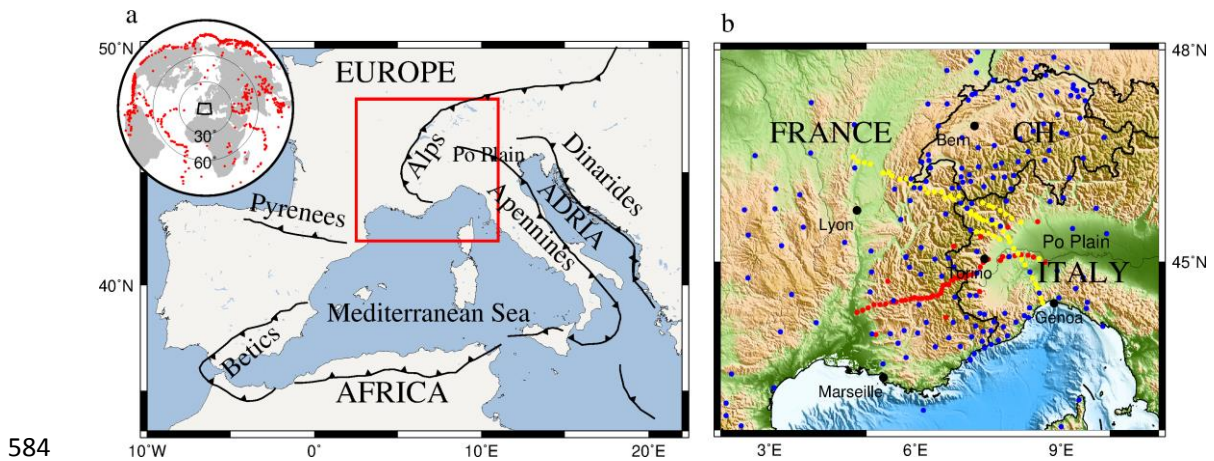
577 Zhu, H., Bozdog, E., Peter, D., Tromp, J., 2012. Structure of the European upper mantle revealed
578 by adjoint tomography. *Nature Geosci.* 5, 493–498.

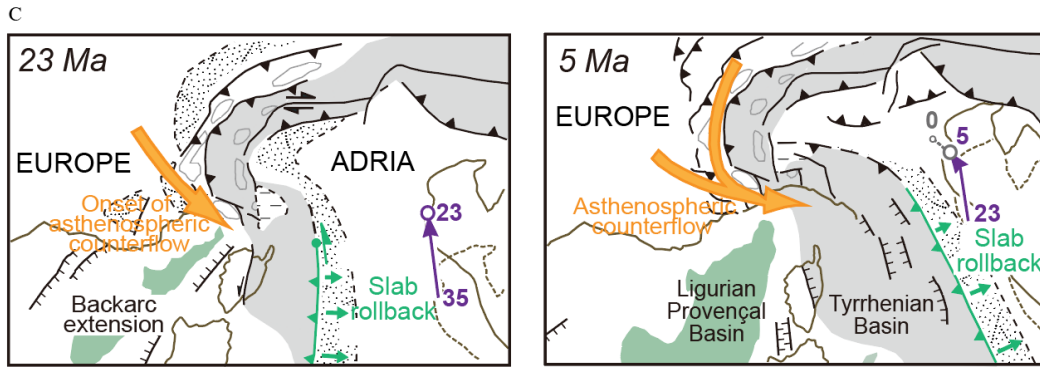
579 Zhu, H., Bozdog, E., Tromp, J., 2015. Seismic structure of the European upper mantle based on
580 adjoint tomography. *Geophys. J. Int.* 201, 18–52.

581 **Figures**

582

583

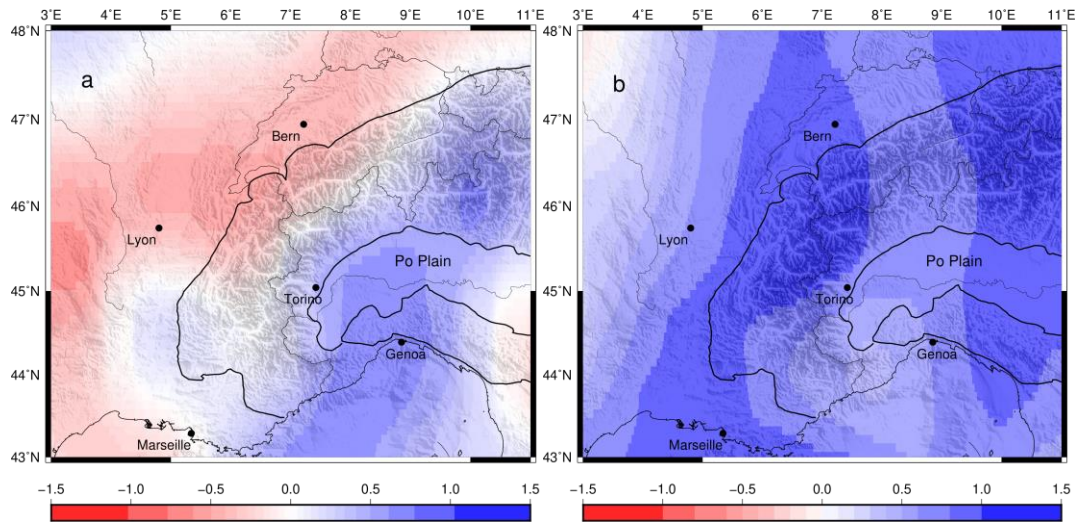




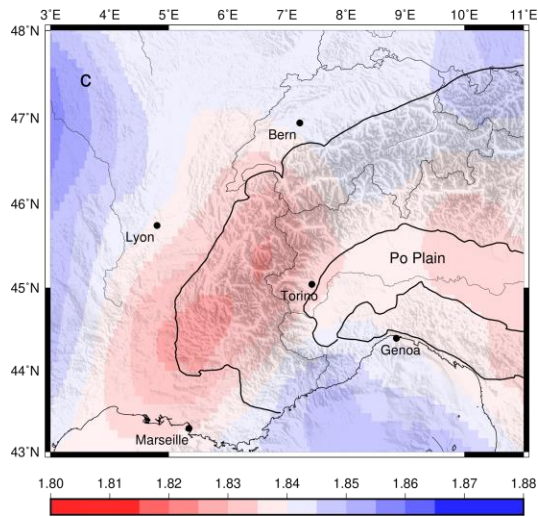
585

586 Fig. 1. (a) Tectonic sketch map of the Adria-Europe plate boundary zone. The red box indicates
 587 the area in frame b. Small inset. Locations of the 1182 teleseismic events used in this study. (b)
 588 Map showing the distribution of the seismic stations used in this study. The red and yellow dots
 589 represent the temporary stations of CICALPS and CICALPS-2, respectively. The blue dots
 590 represent the 193 permanent broadband stations. CH: Switzerland. (c) Neogene evolution of the
 591 Alpine and Apenninic subductions (simplified after Malusà et al., 2021). The gray areas denote
 592 the Alpine metamorphic wedge and the Apenninic accretionary wedge; the purple arrows indicate
 593 the Adria trajectories relative to Europe in the given time interval (in Ma) (from Dewey et al.,
 594 1989); and the orange arrows indicate the direction of the asthenospheric counterflow.

595



596



597

598 Fig. 2. Variations in P-wave velocity (percentages regarding the regional average) at depths of (a)

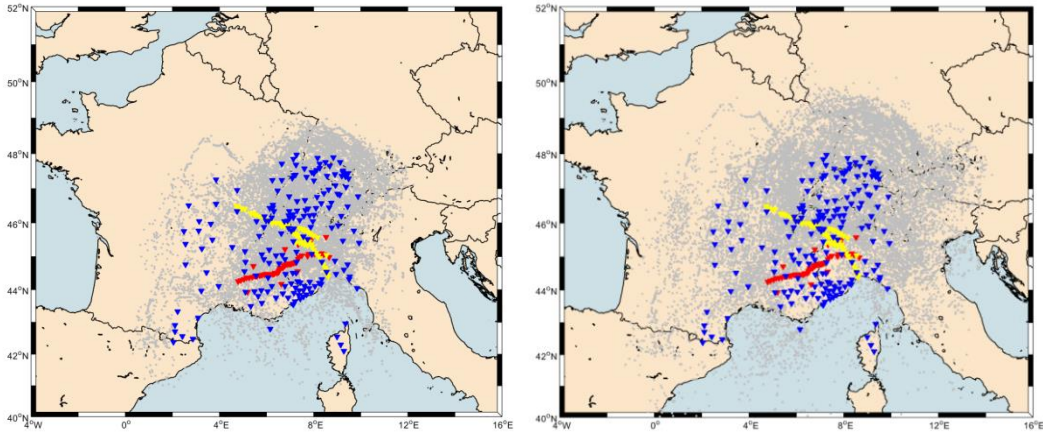
599 410 km and (b) 660 km extracted from the EU60 model. (c) V_p/V_s ratio at depth of 600 km

600 calculated from the absolute P-wave and S-wave velocities of the EU60 model (Zhu et al., 2015).

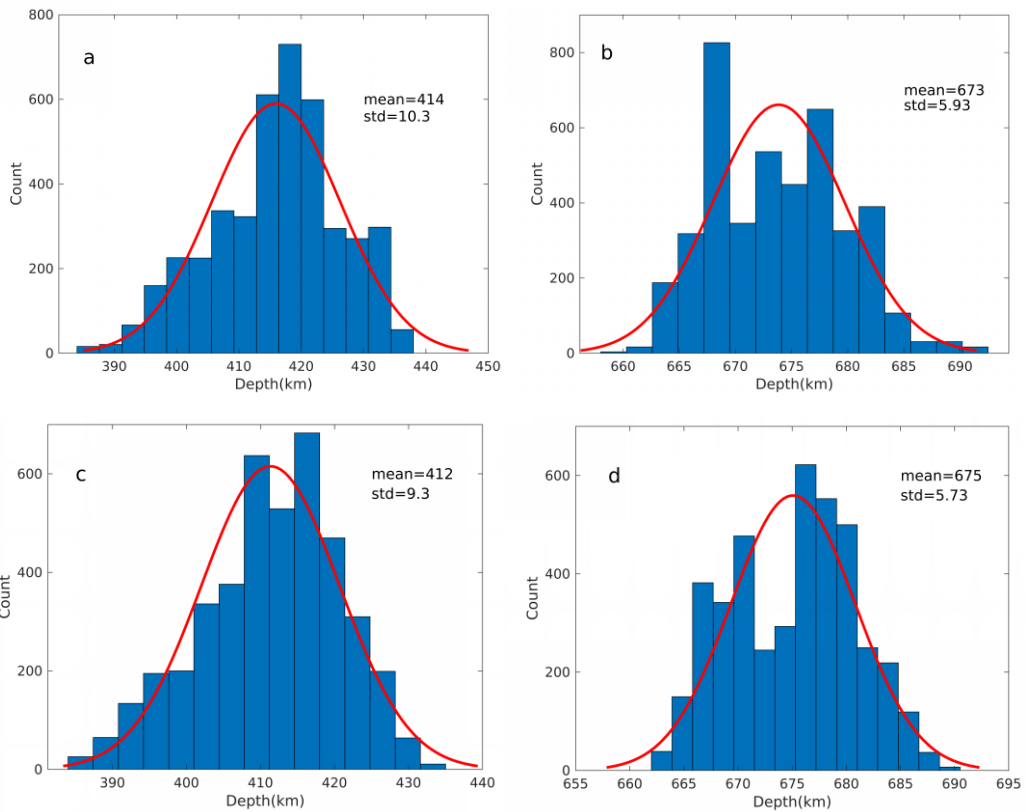
601 The thin black lines are the major tectonic boundaries.

602

603

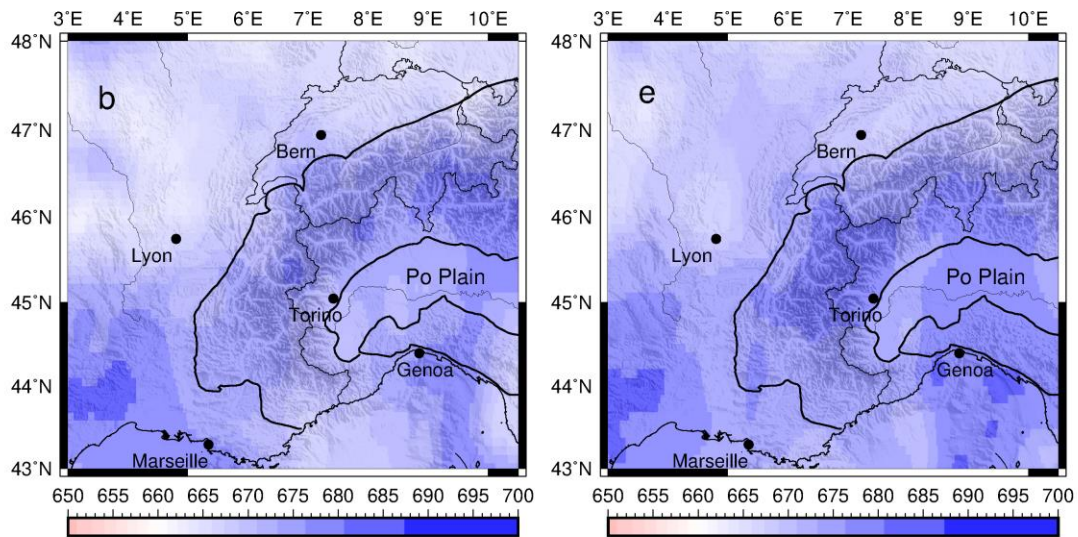
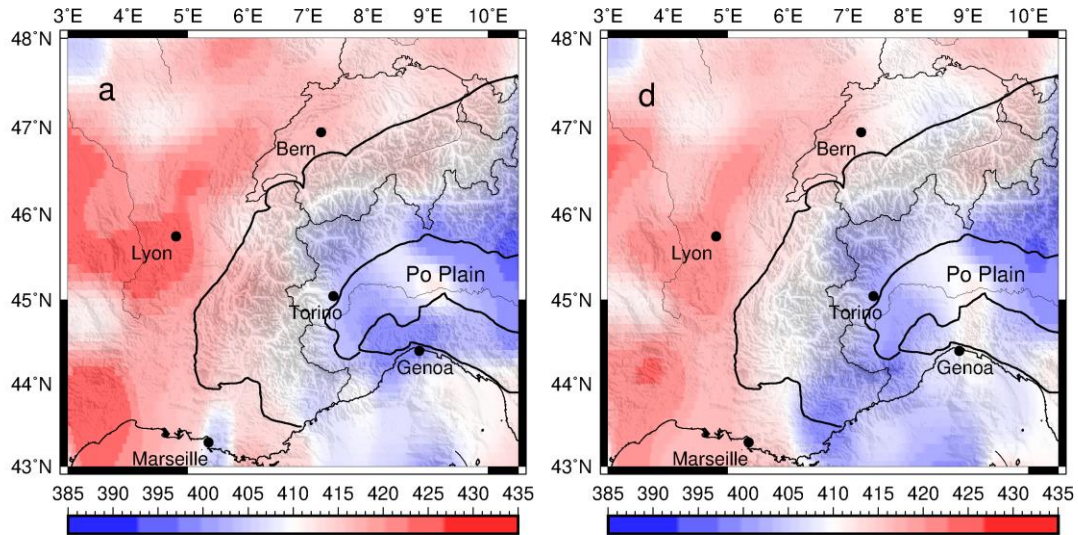


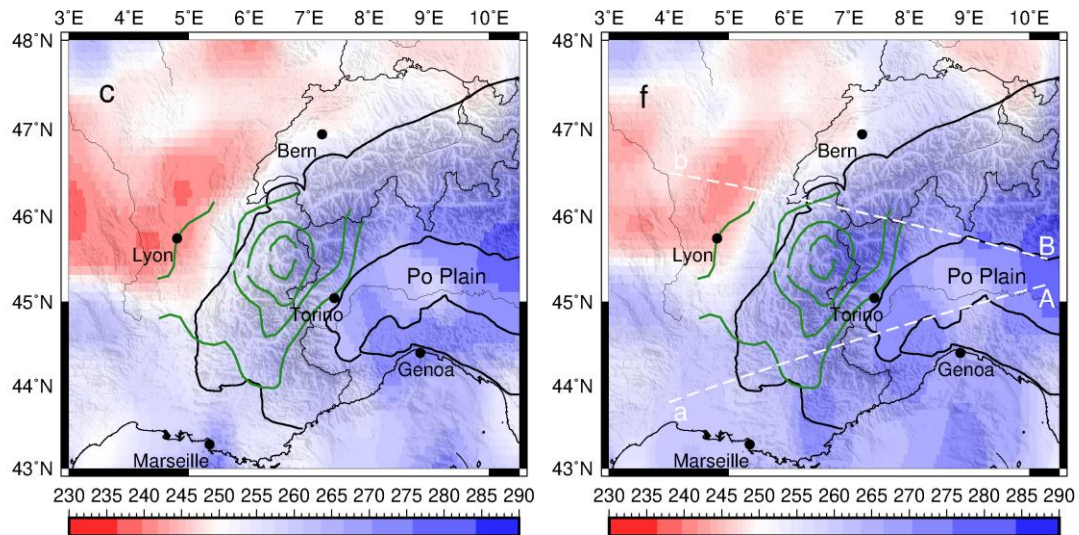
605 Fig. 3. Maps of ray piercing points at depths of (a) 410 km and (b) 660 km computed using the
606 3-D velocity model. The triangles represent the 307 broadband seismic stations. The blue triangles
607 are the 197 stations of the French (FR, RD, G) and Italian (IV, GU) permanent networks. The red
608 and yellow triangles represent the temporary stations of the CIFALPS and CIFALPS-2 projects,
609 respectively.



612 Fig. 4. Distribution of the depth picks of the 410-km discontinuity between 390 and 430 km based

613 on (a) the IASP91 model, and (c) the EU60 model. Distribution of the depth picks of the 660 km
 614 discontinuity between 640 and 710 km based on (b) the IASP91 model and (d) the EU60 model.
 615 The best fit normal distribution is indicated by a red line. The average depth and standard
 616 deviation are indicated (km) in the upper right corner of each panel.





619

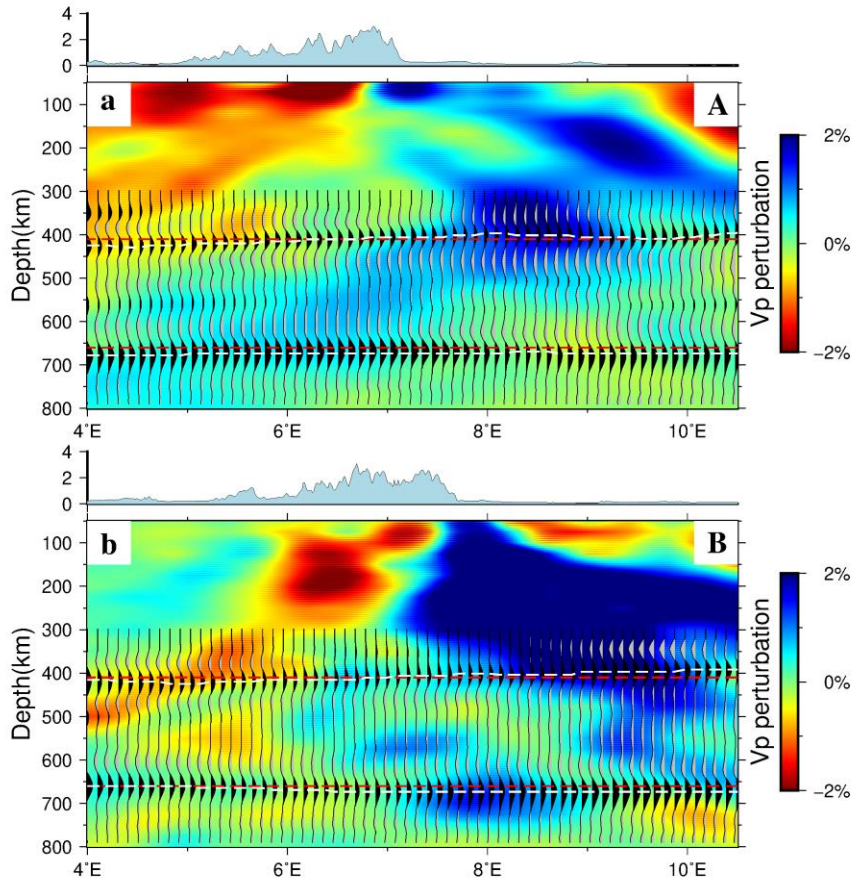
620 Fig. 5. Maps of the depths of the mantle discontinuities and thickness of the MTZ from data

621 migrated using the IASP91 model: (a) 410-km discontinuity, (b) 660-km discontinuity, and (c)

622 thickness of the MTZ, and from data migrated using the EU60 model (d), (e), and (f), as in (a–c).

623 The green lines show the contours of the strong present-day surface uplift rates (Nocquet et al.,

624 2016). The white dashed lines in (f) refer to Fig. 6.



625

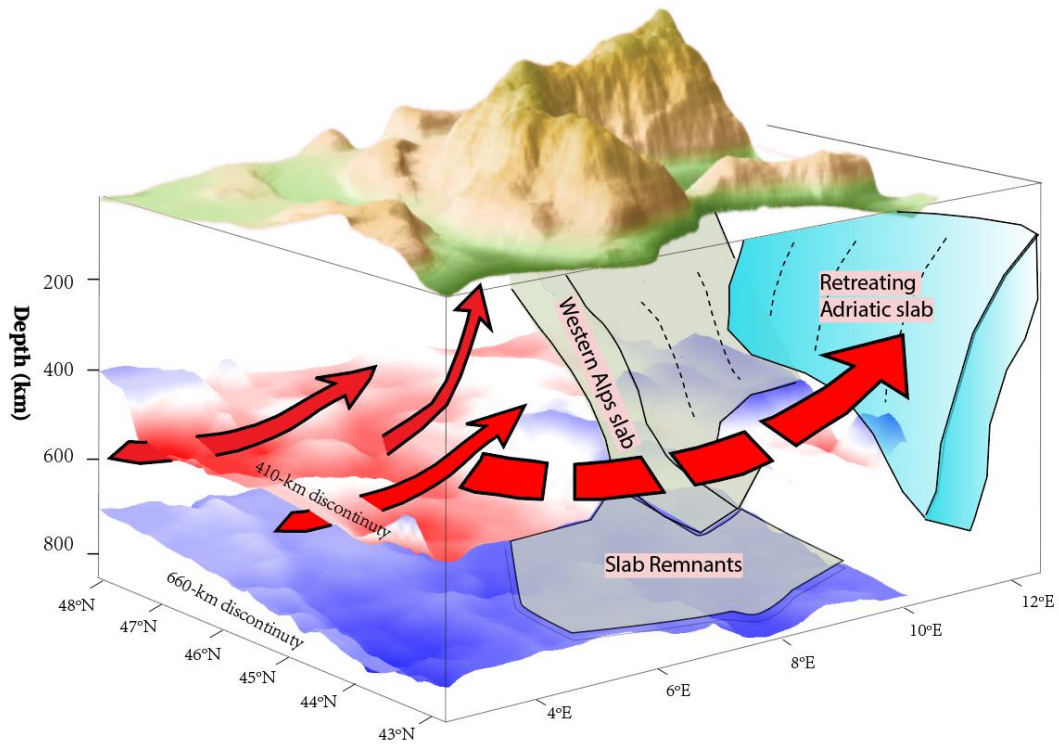
626 Fig. 6. Cross sections through the CCP receiver-function stack with 3-D velocity corrections. The

627 locations of the sections are shown in Fig. 5f. The background is the P-wave velocity perturbation

628 model of Zhao et al. (2016a). The red dashed lines denote the reference depths of 410 and 660 km,

629 and the depths of the maximum amplitudes for the P410s and P660s are indicated by the white

630 dashed lines.

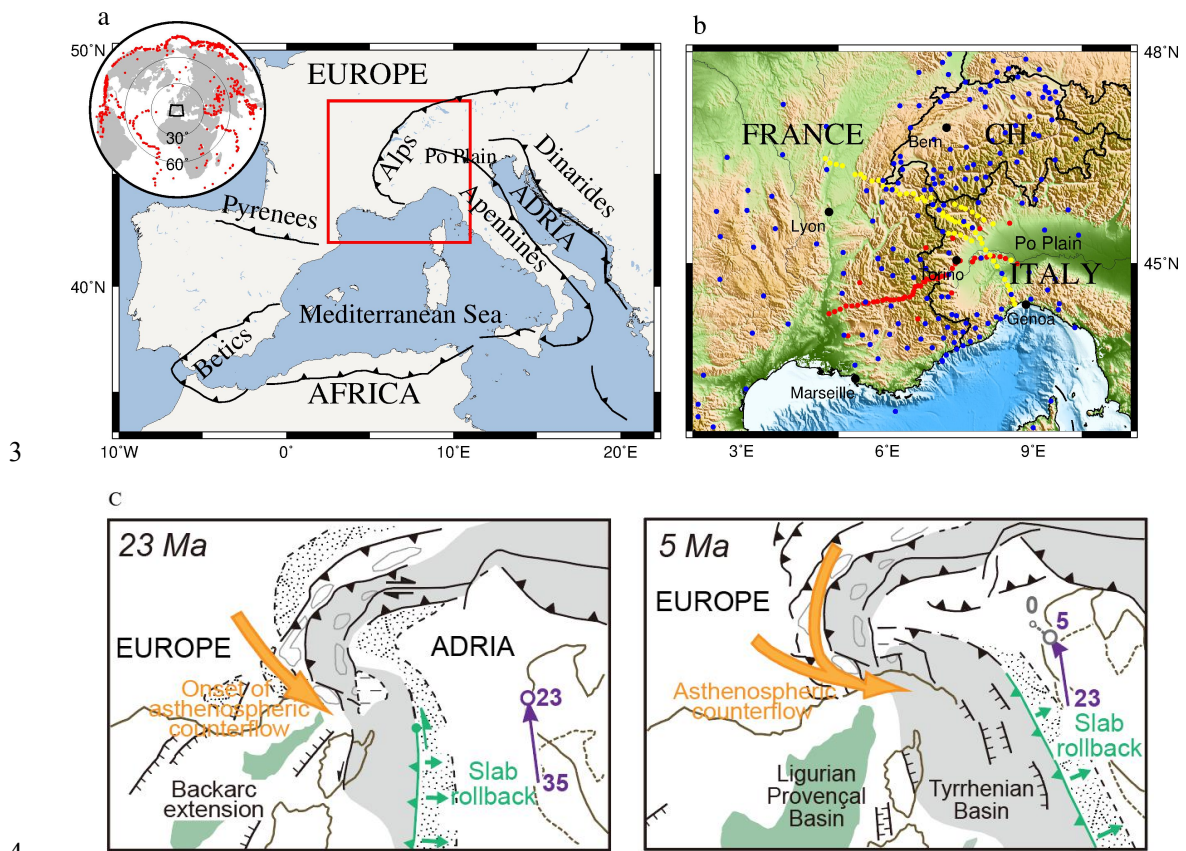


631

632 Fig. 7. A 3-D scheme illustrating the proposed structure and dynamic processes in the upper
 633 mantle beneath the Western Alps according to our observations, the seismic tomography results by
 634 Zhao et al. (2016), and the anisotropy results by Salimbeni et al. (2018). The uplifted 410-km
 635 discontinuity (blue area at longitudes of $>6^{\circ}\text{E}$) indicates that the subducted plate has passed
 636 through the 410-km discontinuity and entered the MTZ. The depression of the 660-km
 637 discontinuity may be related to remnants of subducted oceanic lithosphere. The depressed 410-km
 638 discontinuity (red area) may be related to a thermal anomaly induced by small-scale mantle
 639 upwelling (represented by red arrows), which may have been triggered by downwelling of the
 640 Alpine lithosphere and affected by the rollback of the Apenninic slab to the south.

1 **Figures**

2



3

4

5

6

7

8

9

10

11

12

13

14

15

16

17

18

19

20

21

22

23

24

25

26

27

28

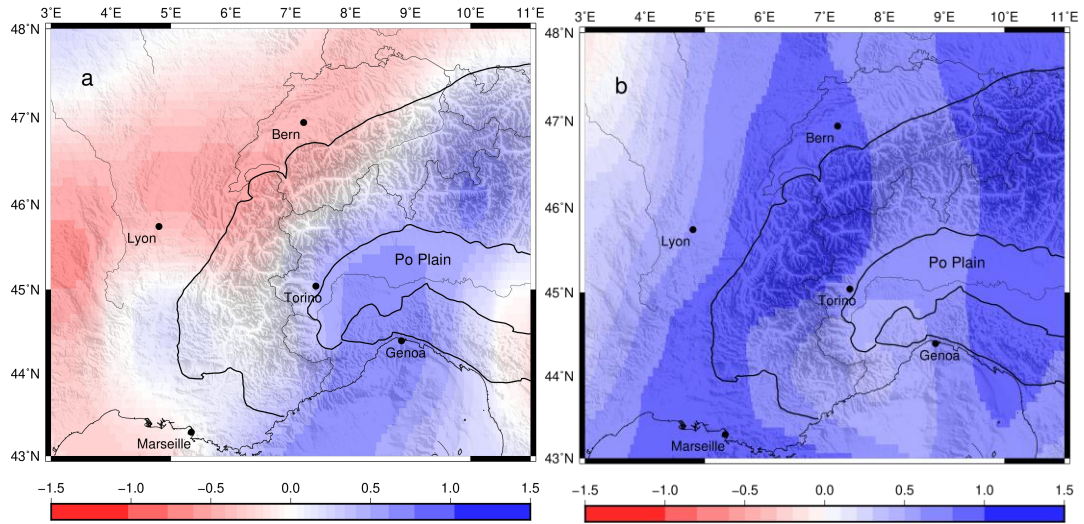
29

30

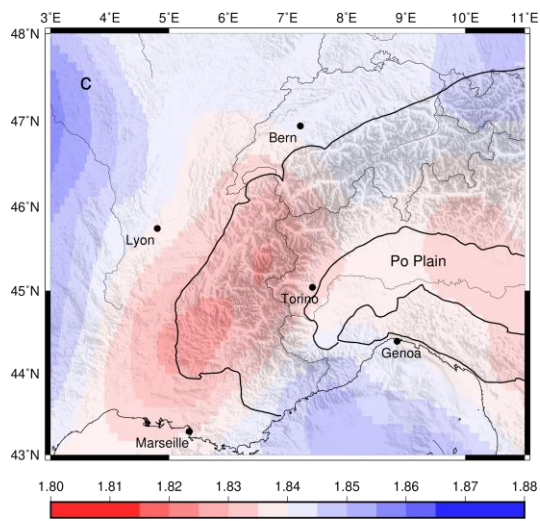
31

32

Fig. 1. (a) Tectonic sketch map of the Adria-Europe plate boundary zone. The red box indicates the area in frame b. Small inset. Locations of the 1182 teleseismic events used in this study. (b) Map showing the distribution of the seismic stations used in this study. The red and yellow dots represent the temporary stations of CIFALPS and CIFALPS-2, respectively. The blue dots represent the 193 permanent broadband stations. CH: Switzerland. (c) Neogene evolution of the Alpine and Apenninic subductions (simplified after Malusà et al., 2021). The gray areas denote the Alpine metamorphic wedge and the Apenninic accretionary wedge; the purple arrows indicate the Adria trajectories relative to Europe in the given time interval (in Ma) (from Dewey et al., 1989); and the orange arrows indicate the direction of the asthenospheric counterflow.



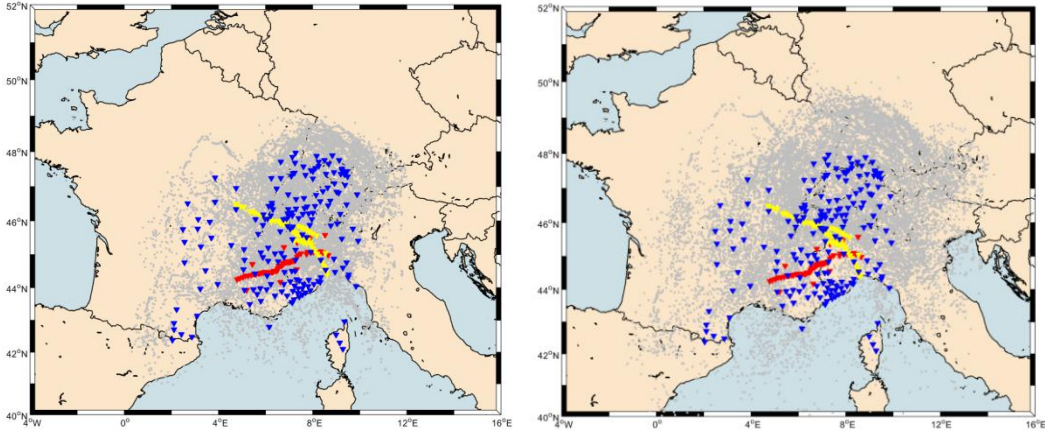
14



15

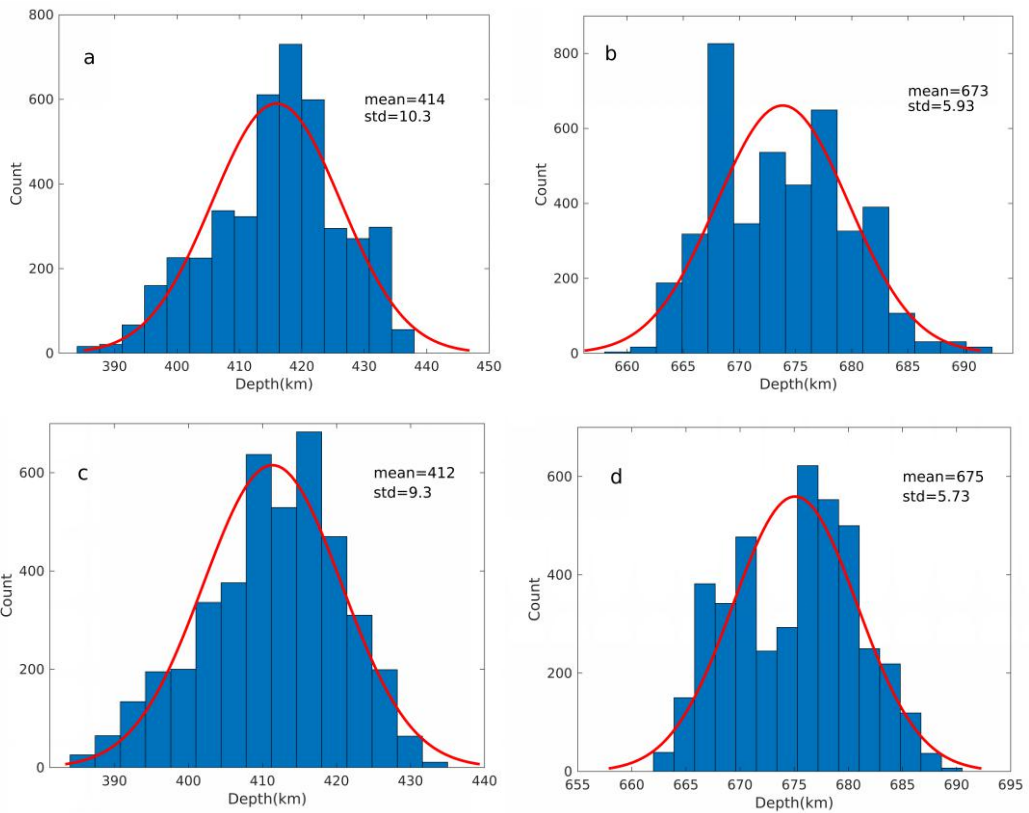
16 Fig. 2. Variations in P-wave velocity (percentages regarding the regional average) at depths of (a)
 17 410 km and (b) 660 km extracted from the EU60 model. (c) V_p/V_s ratio at depth of 600 km
 18 calculated from the absolute P-wave and S-wave velocities of the EU60 model (Zhu et al., 2015).
 19 The thin black lines are the major tectonic boundaries.

20



21

22 Fig. 3. Maps of ray piercing points at depths of (a) 410 km and (b) 660 km computed using the
 23 3-D velocity model. The triangles represent the 307 broadband seismic stations. The blue triangles
 24 are the 197 stations of the French (FR, RD, G) and Italian (IV, GU) permanent networks. The red
 25 and yellow triangles represent the temporary stations of the CIFALPS and CIFALPS-2 projects,
 26 respectively.



27

28

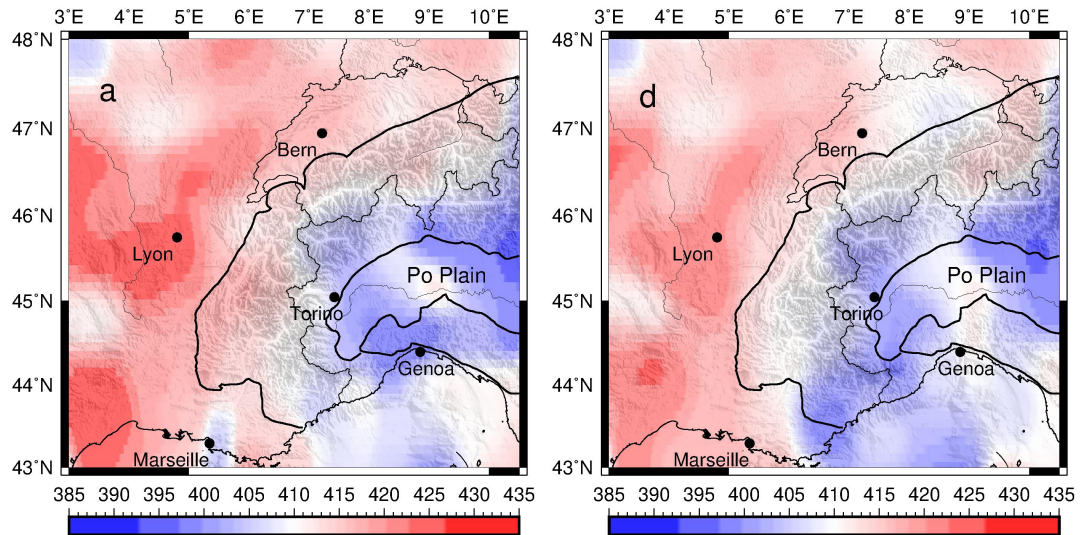
29 Fig. 4. Distribution of the depth picks of the 410-km discontinuity between 390 and 430 km based
 30 on (a) the IASP91 model, and (c) the EU60 model. Distribution of the depth picks of the 660 km

31 discontinuity between 640 and 710 km based on (b) the IASP91 model and (d) the EU60 model.

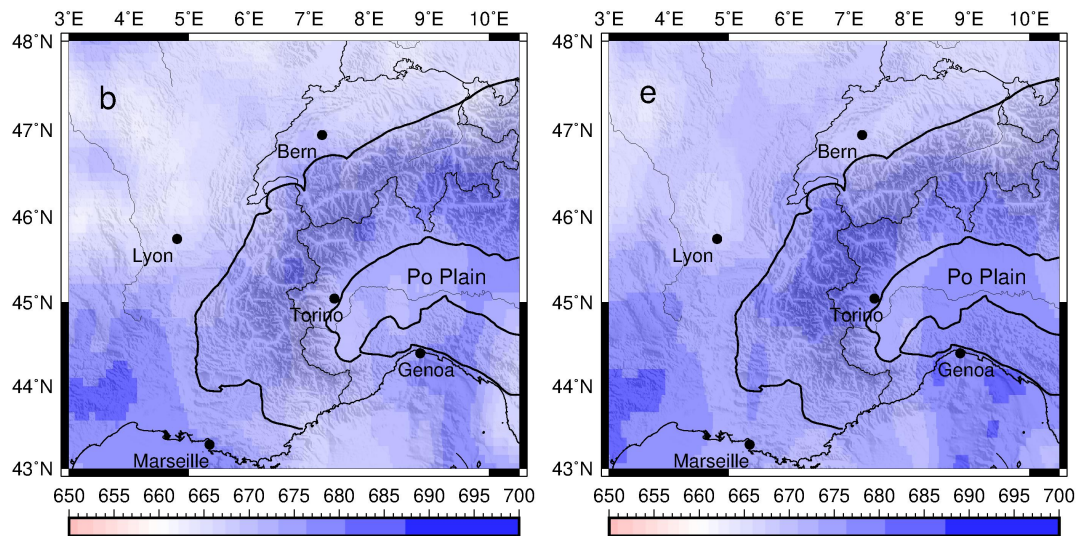
32 The best fit normal distribution is indicated by a red line. The average depth and standard

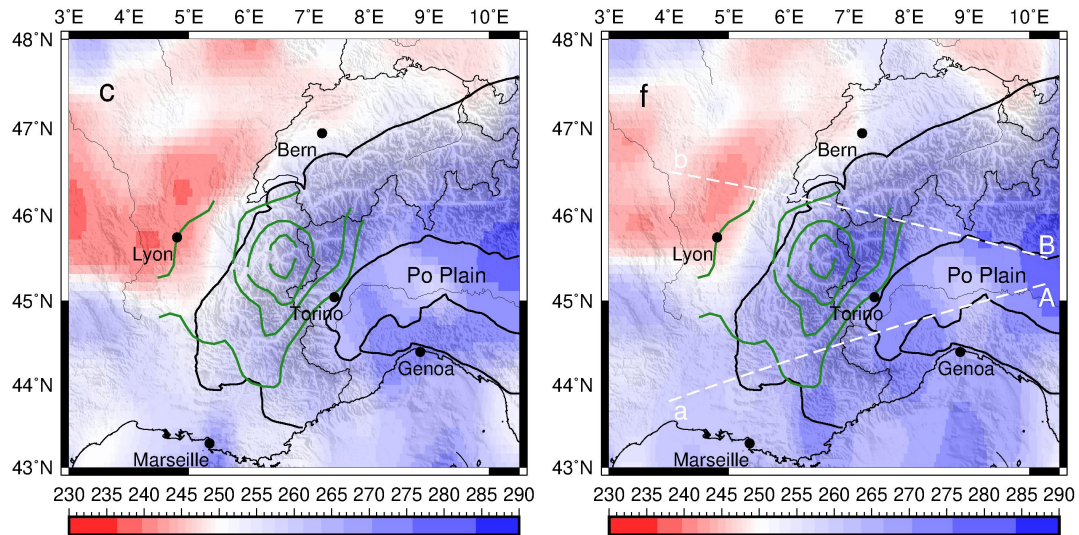
33 deviation are indicated (km) in the upper right corner of each panel.

34



35





36

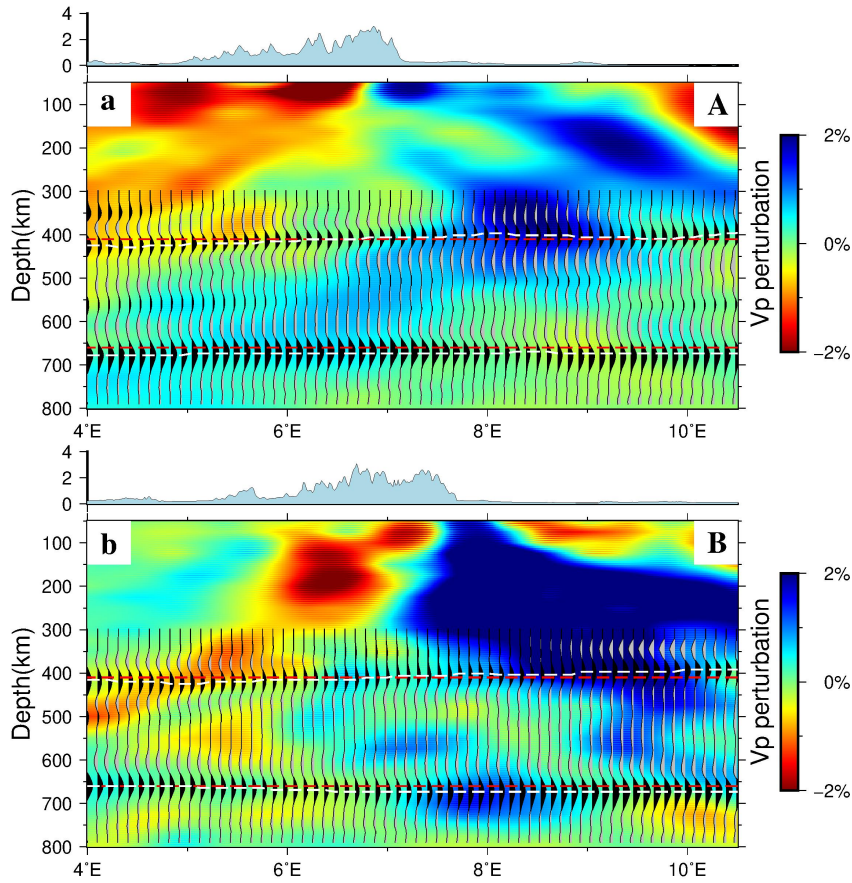
37 Fig. 5. Maps of the depths of the mantle discontinuities and thickness of the MTZ from data

38 migrated using the IASP91 model: (a) 410-km discontinuity, (b) 660-km discontinuity, and (c)

39 thickness of the MTZ, and from data migrated using the EU60 model (d), (e), and (f), as in (a–c).

40 The green lines show the contours of the strong present-day surface uplift rates (Nocquet et al.,

41 2016). The white dashed lines in (f) refer to Fig. 6.



42

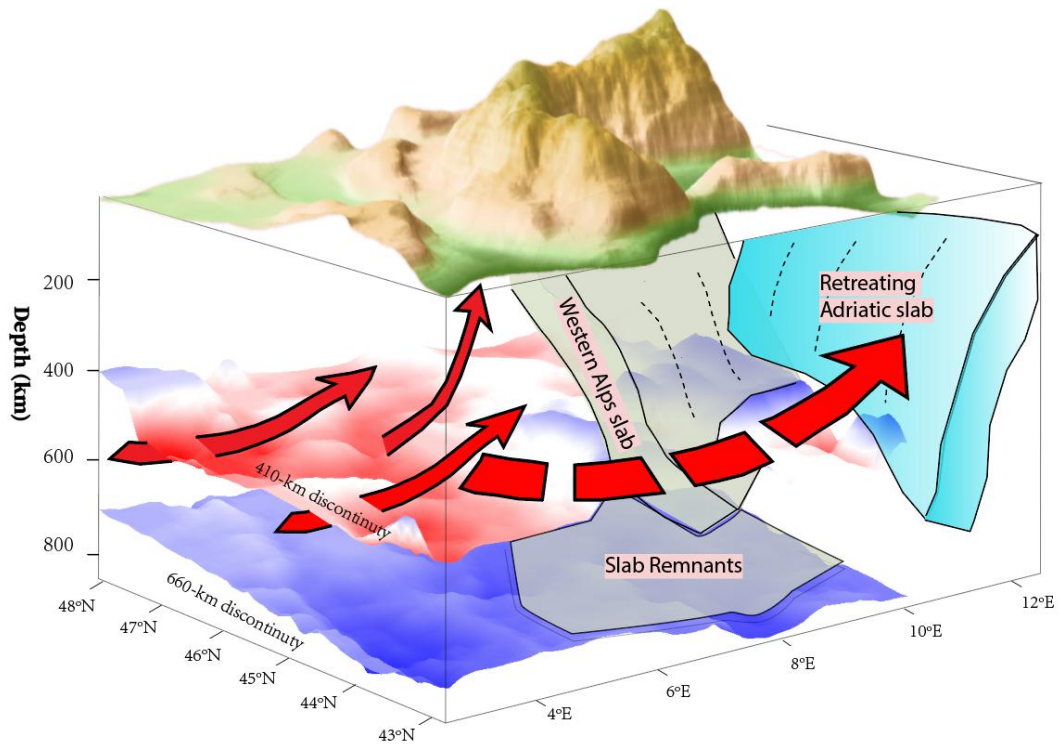
43 Fig. 6. Cross sections through the CCP receiver-function stack with 3-D velocity corrections. The

44 locations of the sections are shown in Fig. 5f. The background is the P-wave velocity perturbation

45 model of Zhao et al. (2016a). The red dashed lines denote the reference depths of 410 and 660 km,

46 and the depths of the maximum amplitudes for the P410s and P660s are indicated by the white

47 dashed lines.



48

49 Fig. 7. A 3-D scheme illustrating the proposed structure and dynamic processes in the upper
 50 mantle beneath the Western Alps according to our observations, the seismic tomography results by
 51 Zhao et al. (2016), and the anisotropy results by Salimbeni et al. (2018). The uplifted 410-km
 52 discontinuity (blue area at longitudes of $>6^{\circ}\text{E}$) indicates that the subducted plate has passed
 53 through the 410-km discontinuity and entered the MTZ. The depression of the 660-km
 54 discontinuity may be related to remnants of subducted oceanic lithosphere. The depressed 410-km
 55 discontinuity (red area) may be related to a thermal anomaly induced by small-scale mantle
 56 upwelling (represented by red arrows), which may have been triggered by downwelling of the
 57 Alpine lithosphere and affected by the rollback of the Apenninic slab to the south.

58